

Exploring the Groß Schönebeck (Germany) geothermal site using a statistical joint interpretation of magnetotelluric and seismic tomography models

Gerard Muñoz*, Klaus Bauer, Inga Moeck, Albrecht Schulze, Oliver Ritter

Deutsches GeoForschungsZentrum (GFZ), Telegrafenberg, 14473 Potsdam, Germany

ARTICLE INFO

Article history:

Received 6 November 2008

Accepted 22 December 2009

Available online 1 February 2010

Keywords:

Geothermal
Exploration
Magnetotellurics
Seismic tomography
Joint interpretation
Groß Schönebeck
Germany

ABSTRACT

Exploration for geothermal resources is often challenging because there are no geophysical techniques that provide direct images of the parameters of interest, such as porosity, permeability and fluid content. Magnetotelluric (MT) and seismic tomography methods yield information about subsurface distribution of resistivity and seismic velocity on similar scales and resolution. The lack of a fundamental law linking the two parameters, however, has limited joint interpretation to a qualitative analysis. By using a statistical approach in which the resistivity and velocity models are investigated in the joint parameter space, we are able to identify regions of high correlation and map these classes (or structures) back onto the spatial domain. This technique, applied to a seismic tomography-MT profile in the area of the Groß Schönebeck geothermal site, allows us to identify a number of classes in accordance with the local geology. In particular, a high-velocity, low-resistivity class is interpreted as related to areas with thinner layers of evaporites; regions where these sedimentary layers are highly fractured may be of higher permeability.

© 2010 Elsevier Ltd. All rights reserved.

1. Introduction

The non-uniqueness of the inverse problem in geophysics, together with an incomplete knowledge of the subsurface and the varying spatial resolution of derived models, makes it difficult to interpret geophysical data directly in terms of geological units. The inversion models provide the spatial distribution of a physical parameter (e.g. electrical resistivity, seismic velocities, magnetic susceptibility), which is then commonly used as a proxy for a rock property in the area under investigation (e.g. porosity, mineral composition, fracture density). This interpretation is not always straightforward, because the physical parameters do not depend on a single property but on a (possibly complex) combination of several properties. For example, seismic velocity is not only controlled by mineral composition but also by temperature, pressure, pore space geometry and other rock properties, while electrical resistivity depends on rock porosity, fluid saturation, salinity, temperature, etc. (It is assumed hereunder that the cause of low resistivity is the presence of saline fluids, but it could be due to the existence of ore minerals, partial melt, or conductive clays.)

Therefore, it is common to use a combination of geophysical methods to obtain the distribution of independent physical properties over the area of interest in order to discriminate between

the different possible geologic/lithologic units. This kind of study, however, is usually limited to a qualitative comparison of the different models, which may – or may not – yield a relation between the parameters in certain regions.

Quantitative approaches are usually based on either joint inversion of two independent data sets or on empirical or constitutive relations between the physical parameters. Approaches to joint inversion often include geometrical constraints, such as the requirement of coincident interfaces (e.g. Moorkamp et al., 2007) or the use of physical properties gradients (cross gradients inversion) to characterize the geometrical features of the models (Gallardo and Meju, 2007). Combined interpretations, and some joint inversion approaches, commonly link different geophysical parameters through rock property models. These models assume that a certain relation between the modelled physical parameters and the properties of interest (porosity, water saturation, etc.) is valid under particular conditions and, therefore, require local calibration, e.g. with borehole data. These local relationships can then be used, for example, as constraints for a joint inversion (Colombo et al., 2008) or to derive reservoir parameters via Bayesian inversion (Hoversten et al., 2005).

The magnetotelluric (MT) and seismic methods are the only geophysical exploration techniques that can yield reliable images at depths greater than the km-scale. The MT and seismic tomography techniques provide images of electric resistivity (ρ) and seismic velocity (V_p , V_s), respectively, with similar spatial resolution (e.g. Jones, 1987; Unsworth and Bedrosian, 2004) and are

* Corresponding author. Tel.: +49 331 288 1258; fax: +49 331 288 1266.

E-mail address: gmunoz@gfz-potsdam.de (G. Muñoz).

Nomenclature

$\text{pdf}(\rho, V_p)$	joint probability density function of the resistivity–seismic velocity distribution
V_p	P-wave seismic velocity (m/s)
m	number of parameter points in the joint parameter space
$\text{pdf}_i(\rho, V_p)$	probability density function of the i th parameter pair (ρ, V_p) of the joint resistivity–seismic velocity distribution
$V_{p,i}$	seismic velocity of the i th element of the parameter space (m/s)
$\delta \log(\rho_i)$	error of the electrical resistivity of the i th element of the parameter space
$\delta V_{p,i}$	error of the P-wave seismic velocity of the i th element of the parameter space (m/s)
$C_{\log(\rho)}$	mean error of $\log(\rho)$
s_i	normalized sensitivity of the electrical resistivity of the i th element of the parameter space
$\overline{\log(s)}$	average of the sensitivity of the electrical resistivity over all m parameters of the parameter space
C_{V_p}	mean error of V_p (m/s)
n_i	hit counts (number of rays crossing a particular cell) in the cell corresponding to the i th element of the parameter space
$\overline{\log(n)}$	average of the hit counts over all m parameters of the parameter space
$f(\mathbf{x})$	function representing the best fit to $\text{pdf}(\rho, V_p)$, is a sum of n bivariate Gaussian peaks
$\mathbf{x} = [\log(\rho), V_p]$	vector representing a pair resistivity–seismic velocity in the joint parameter space
n	number of bivariate Gaussian peaks in f
a_j	amplitude of the j th Gaussian function composing f
Greek letters	
μ_j	centre of the j th Gaussian function composing f
ρ	electrical resistivity ($\Omega \text{ m}$)
ρ_i	electrical resistivity value of the i th element of the parameter space ($\Omega \text{ m}$)
Σ_j	covariance matrix of the j th Gaussian function composing f

often used in combination to derive models of the subsurface (e.g. Jones, 1998; Mechie et al., 2004; Maercklin et al., 2005; Unsworth et al., 2005). Both methods have their characteristic limitations. Magnetotellurics, for example, has an inherent loss of resolution with depth because it is based on diffusive fields. It has particular difficulty resolving structures located below good conductors due to the energy dissipated within them. Seismic refraction has trouble imaging vertical contrasts. By looking at both resistivity and velocity at the same time, we can build on the strengths of both methods and mitigate their weaknesses.

The problem with a joint MT–seismic tomography interpretation is that there is no unique or universal law linking electrical resistivity (ρ) and seismic velocity (V_p or V_s). Roughly speaking, while in a sedimentary environment electrical resistivity is mostly sensitive to the fluid phases present in the rock pores and/or fractures, seismic velocity is mainly imaging rock matrix properties. However, using a statistical analysis of the distributions of both resistivity and velocity, we can find certain areas in the models where a particular relation between physical parameters holds locally, thus allowing us to characterize this region as having a particular lithology.

Here, we use a statistical analysis, as described by Bedrosian et al. (2007) in order to correlate two independently obtained models (a V_p tomography model and an electrical resistivity model) of the Groß Schönebeck geothermal test site.

2. Methodology

The approach of Bedrosian et al. (2007) is based on a probabilistic method developed by Bosch (1999) whose premise is that diverse geophysical parameters are represented as a probability density function (pdf) in the joint parameter space. The coincident velocity and resistivity models are first interpolated onto a common grid. Therefore, a joint parameter space is built, where each point in the modelled area is associated with a velocity–resistivity pair. By plotting one parameter against the other in a cross-plot and including the error estimates we can then construct a joint pdf in the parameter space.

The areas of enhanced probability can be identified as classes that are represented by a certain range in both resistivity and velocity values. By mapping back these classes onto the spatial domain they can be related to particular lithologies and/or geological units. A similar approach has been used in different contexts and with different pairs of physical parameters. Bauer et al. (2003) combined seismic velocity and Poisson's ratio in order to establish a lithologic classification for an igneous complex in Namibia. Haberland et al. (2003) used electrical resistivity and seismic attenuation models to define regions of partial melting beneath the southern Bolivian Altiplano plateau, and Bedrosian et al. (2004) investigated the San Andreas Fault (USA) utilizing a combination of MT and seismic models.

Below we present a brief overview of the methodology; a more detailed analysis can be found in Bedrosian et al. (2007).

2.1. Interpolation

Before the joint pdf for both physical parameters can be assembled, the two sets of model values must be evaluated on a common grid. This is a crucial step because it is important to establish that the estimated and original point distributions are statistically similar. At the same time, one wants to avoid loss of information and creation of artefacts during the interpolation process. As the two models will be, in general, on different model meshes or grids, there are basically three options: the resistivity values can be interpolated onto the velocity grid, the velocity values can be interpolated onto the resistivity grid, or both parameters can be interpolated onto an independent grid. The latter option is rejected, because it involves an additional step, and one wants to keep the number of interpolations to a minimum.

An important difference between MT and seismic models is the discretization of the grids being used. For seismic models, the grids are commonly uniformly spaced. Due to the diffusive nature of the electromagnetic (EM) fields, which decay exponentially with distance (Vozoff, 1987), MT model grids are usually non-uniform, coarsening with depth and distance from the measurement points. In addition, seismic velocity models usually contain more mesh points than electrical resistivity models. Therefore, the interpolation of the velocity values onto the resistivity grid involves a net loss of velocity information. Taking into account that a uniform grid is desirable to ensure that all parts of the model are equally represented, the interpolation of the resistivity values onto the velocity mesh is chosen.

Interpolation of scatter points can be performed in a variety of ways, as described in standard geostatistical texts (e.g. Isaaks and Srivastava, 1989). We used an inverse distance weighted (IDW) interpolation that gives estimates from a weighted average of many

samples found within a pre-defined area (or buffer) around scatter points, with decreasing weight with distance. Several weights were tested, with fixed buffers, as well as with buffers changing with depth, and the estimated point distributions were compared against the initial ones through cross-validation. The distribution of the residuals gives an idea of the accuracy of the interpolated resistivity model.

When performing the interpolation, it is very important to ensure that the relative frequency of the resistivity distribution in the interpolated model is very close to the relative frequency of the parameters in the original model. Otherwise, even if the residuals are minimal, the resulting joint probability density function (see below) can be inaccurate and may, therefore, result in an erroneous cluster classification.

2.2. Model correlation

Once both data sets are on a common grid, the ensemble can be thought of as a joint parameter space, where each grid point i is identified by a resistivity–velocity pair. Each of the m elements of this distribution can be interpreted as the outcome of a process defined by a probability density function (pdf). Assuming a normal error distribution and independence of the data, the joint pdf is expressed as the sum of the individual probability density functions (pdf _{i}) for each data point, according to:

$$\text{pdf}(\rho, V_p) = \frac{1}{m} \sum_{i=1}^m \text{pdf}_i(\rho, V_p) \quad (1)$$

$$\text{pdf}_i(\rho, V_p) = \frac{1}{\sqrt{2\pi\delta \log(\rho_i)\delta V_{p,i}}} \times \exp \left[-\frac{1}{2} \left[\frac{(\log(\rho) - \log(\rho_i))^2}{\delta \log(\rho_i)^2} + \frac{(V_p - V_{p,i})^2}{\delta V_{p,i}^2} \right] \right] \quad (2)$$

where $\delta \log(\rho_i)$ and $\delta V_{p,i}$ are the errors of the individual electrical resistivity and P-wave velocity values, respectively. Therefore, to assemble the joint pdf, an estimate of the errors of the individual model parameters is needed.

In MT an estimate of the parameter errors can be obtained from the Jacobian (or sensitivity) matrix of the linearized forward problem, which contains the partial derivatives of the data with respect to the model parameters. Schwalenberg et al. (2002) suggested using column-wise sums (for all data points) of the Jacobian matrix, normalized by the measurement error in each data point, to estimate the relative sensitivity of the individual parameters. Therefore, the errors $\delta \log(\rho_i)$ are calculated according to:

$$\delta \log(\rho_i) = C_{\log(\rho)} \left[\frac{\overline{\log(s)}}{\log(s_i)} \right] \quad (3)$$

where s_i is the normalized sensitivity of a given parameter in the sense of Schwalenberg et al. (2002), and $C_{\log(\rho)}$ the mean error in $\log(\rho)$. The bar over $\log(s)$ indicates an average over all model parameters. It is important to note that this approach is a linear sensitivity analysis, only accounting for small model perturbations. It, however, provides a rough estimate of the resistivity errors that can be used in the calculation of the pdf.

In seismic tomography the relative velocity errors are estimated from ray coverage, according to:

$$\delta V_{p,i} = C_{V_p} \left[\frac{\overline{\log(n)}}{\log(n_i)} \right] \quad (4)$$

where n_i is the number of hit counts in a given cell, and C_{V_p} the mean velocity error. Here, again, the overline indicates an average

over all model points. The mean errors $C_{\log(\rho)}$ and C_{V_p} have to be determined from the scatter plot of velocity versus log resistivity; see Bedrosian et al. (2007) for details.

To summarize, the joint parameter space is represented by a joint probability density function (pdf) that shows higher values in areas were particular values of resistivity and velocity cluster.

2.3. Classification

The basis of the classification scheme is the assumption that the lithologic/geologic units are spatially connected domains characterized by uniform physical properties normally distributed. It is, therefore, possible to distinguish between two units in the joint pdf if the contrast between physical properties is greater than the estimated errors. In practice, the different classes (or structures) are identified as zones of enhanced probability in the joint pdf cross-plot. Based on the assumption that each class is normally distributed, defined by a mean point and a covariance matrix (representing the ~60% confidence interval ellipse for the peak) in the joint parameter space, we define the classes as n bivariate Gaussian functions.

The parameters defining the Gaussian functions are calculated by fitting the joint pdf to the function:

$$f(\mathbf{x}) = \sum_j^n \frac{a_j}{2\pi|\Sigma_j|^{1/2}} \exp -\frac{1}{2} \left[(\mathbf{x} - \mu_j)^T \Sigma_j^{-1} (\mathbf{x} - \mu_j) \right] \quad (5)$$

where $\mathbf{x} = [\log(\rho), V_p]$, a_j are the amplitudes, μ_j the centres, and Σ_j the covariance matrices for the n Gaussian peaks (classes) that best fit the joint pdf, the superscript T means matrix transpose.

The user picks manually the number of classes and the initial values for the iterative fitting process from the joint pdf cross-plots. The convergence of this process is very sensitive to the starting parameters and thus their manual selection, which sets them close to the assumed values, improves the convergence and aids in peak separation.

However, in some cases it can happen that the best fitting solution produces a considerable overlap between two or more classes. In that case it is difficult to determine to which class a certain parameter belongs. Then, it is advisable to use the classes determined manually by the user, however, this introduces greater subjectivity to the process.

2.4. Synthetic example

In order to demonstrate the employed methodology, we present its application to a synthetic model (Fig. 1a) that consists of a low-resistivity, low-velocity layer (1) overlaying a vertical contact marking a contrast in resistivity and velocity (2–3). Within the lower right space (3), a high-velocity, high-resistivity body is embedded (4). Fig. 1b shows the joint pdf of both models in a gray-scale-shaded plot, with darker areas representing regions of enhanced probability; four clusters can be clearly identified (coloured ellipses). The gradient in velocity causes the clusters to be elongated along the velocity axis. Fig. 1c shows the back-mapping of the clusters onto the spatial domain where they recover the structures of the original models.

Fig. 1d depicts the models obtained from the inversion of the synthetic responses of the models in Fig. 1a with 2.5% Gaussian noise added. This inversion models highlight how the application of the joint interpretation reinforces the weaknesses of both methods. Namely, the seismic model does not reliably resolve the vertical contrast and the resistivity model does not reliably resolve the deeper high-velocity, high-resistivity body.

The joint pdf of both inversion models is given in Fig. 1e. The smoothing in both seismic and MT inversion causes the clusters

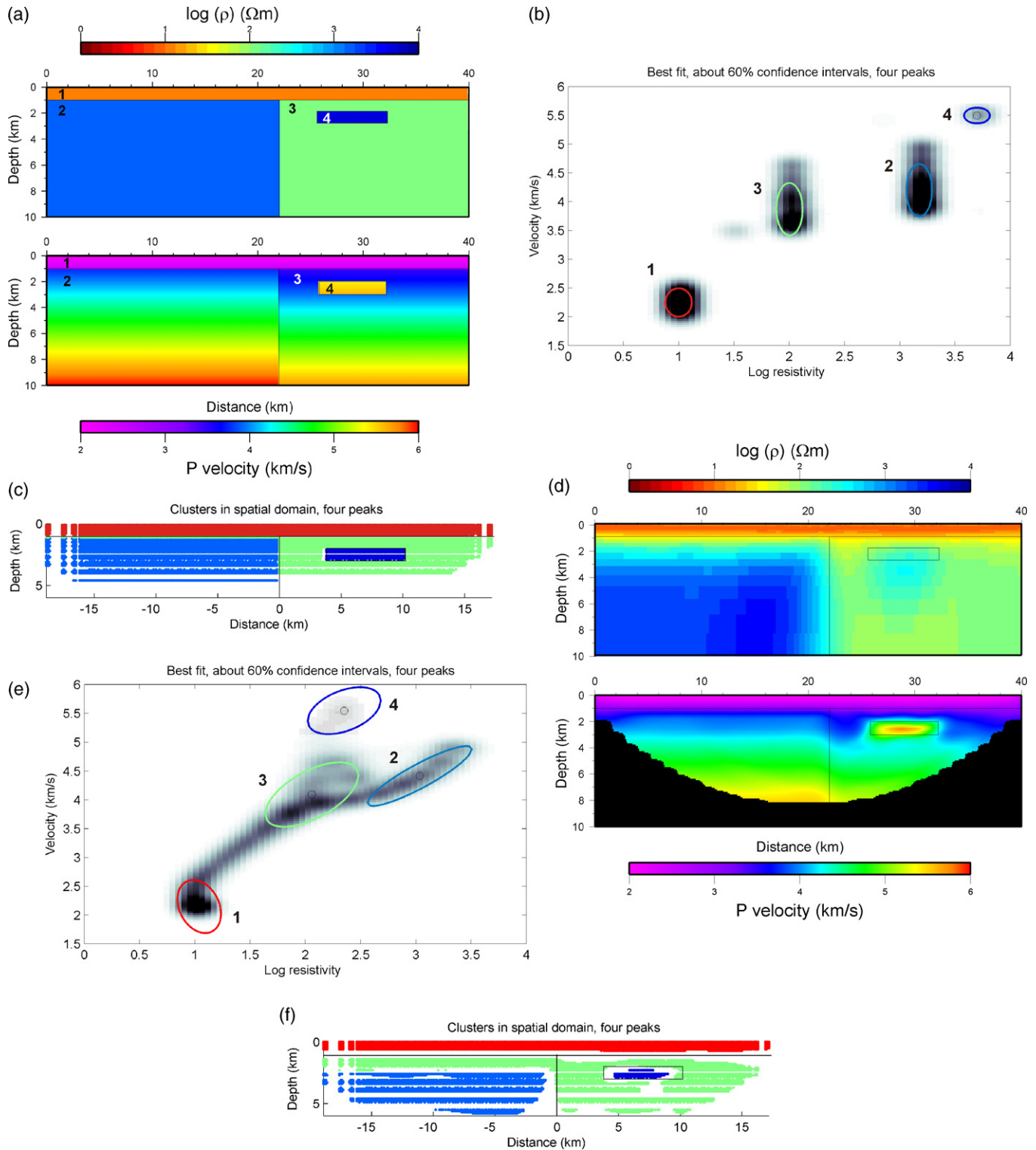


Fig. 1. Synthetic example illustrating the methodology used in the study of the Groß Schönebeck geothermal test site. (a) Starting resistivity and velocity models consisting of a low-resistivity, low-velocity layer (1) overlying a vertical contact marking a contrast in resistivity and velocity (2–3); within the lower right space (3), a high-velocity, high-resistivity body is embedded (4); (b) joint pdf of both models in a gray-scale-shaded plot, with darker areas representing areas of enhanced probability; four clusters (coloured ellipses) can be clearly identified; (c) back-mapping of the clusters onto the spatial domain where they recover the structures of the original models; (d) models obtained from the inversion of the synthetic responses of the models in (a) with 2.5% Gaussian noise added; (e) joint pdf of both inversion models; (f) back-mapping back of the clusters onto the spatial domain recovers the original structures even though the individual inversions were not able to resolve either the vertical contrast 2–3 (seismic tomography) or the high-velocity, high-resistivity body 4 (MT).

to be elongated along both the velocity and resistivity axes. It is clear from the clustering that the overburden (1) is detected by both methods (the red ellipse presents ρ and V_p values different from those of all other clusters). The two quarter spaces (2

and 3) are only separated in the resistivity model (the green and blue ellipses cover the same velocity range but different, non-overlapping resistivity ranges). The cluster associated with the high-velocity, high-resistivity body (4) has changed position in the

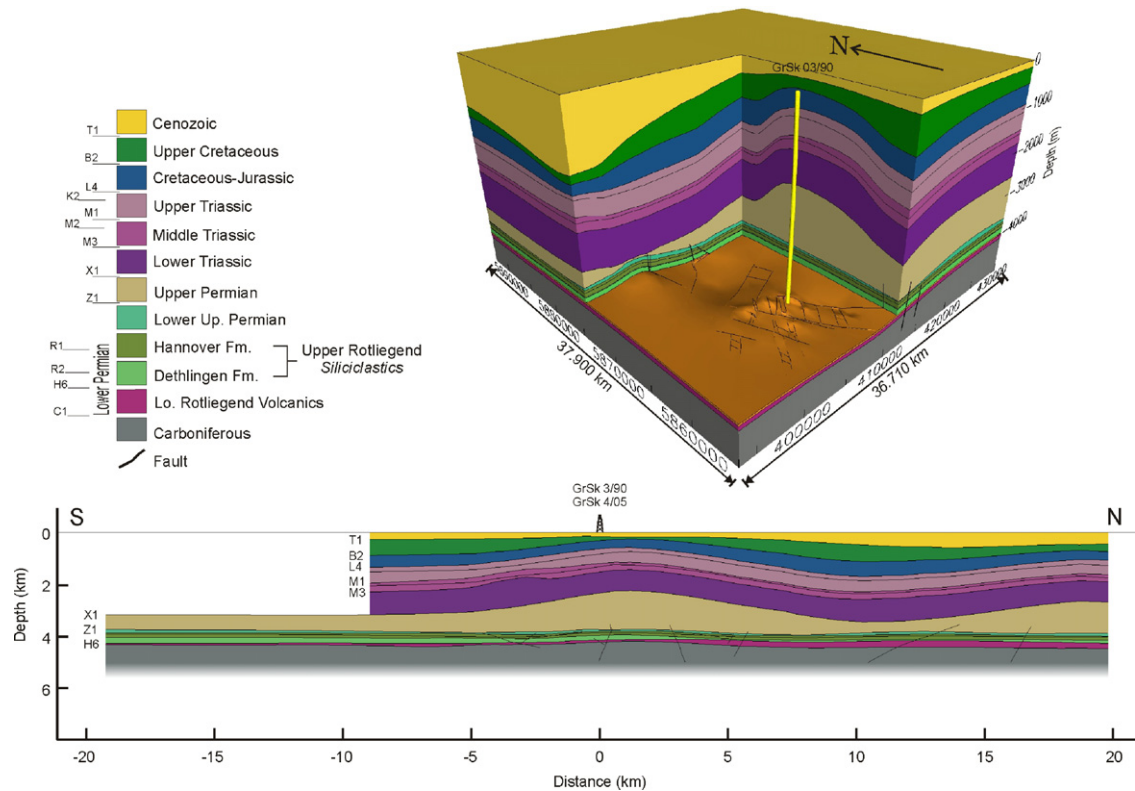


Fig. 2. Three-dimensional geological model Groß Schönebeck geothermal test site developed from seismic refraction and well-log data (after Moeck et al., 2008). The yellow line in the top block corresponds to the trace of well GrSk 3/90 (top). The cross-section at the bottom is drawn along the seismic-MT profile (bottom).

cross-plot with respect to the joint pdf of the initial models (Fig. 1b), and it is only distinguishable from the corresponding quarter space (3) by its velocity value.

Fig. 1f shows that mapping back the clusters onto the spatial domain recovers the original structures even though the individual inversions were not able to resolve either the vertical contrast 2–3 (seismic tomography) or the high-velocity, high-resistivity body 4 (MT). It is only after the classification in the joint parameter space that the four structures can be clearly determined.

3. Geophysical models

The Groß Schönebeck low-temperature geothermal site, with its well doublet GrSk 3/90 and GrSk 4/05, is located in the North-east German Basin (NEGB). It corresponds to the eastern part of the North German Basin that has a complex polyphase history since the Lower Permian (Scheck and Bayer, 1999; Scheck et al., 1999).

The probable geothermal reservoir is hosted, on average, in 400 m of sedimentary rocks that overlie 60 m of volcanics (Rotliegend of the Lower Permian). These units are located below thick (>1000 m) evaporite layers of the Upper Permian (Zechstein) that comprise a mixture of shales, carbonates, anhydrite and salt rock. The mobility of the evaporites that results in the formation of salt ridges, diapirs and salt lows (Fig. 2) affects the structure of the Mesozoic and Cainozoic overburden. In particular, the structure and nature of the reservoir rocks is highly differentiated due to local depositional centres in the NEGB that existed during the Lower Permian.

The detection of high-permeability zones is one of the most important issues in geothermal exploration, which, however, are not sufficiently resolved in the existing geological models (Moeck et al., 2008). As we will show, the combination of densely sampled MT and seismic data can contribute to clarify the location of effective potential geothermal reservoir rocks.

3.1. Magnetotelluric model

Magnetotelluric data were collected along a 40 km-long profile centred on the Groß Schönebeck well doublet (Fig. 3). It consists of 55 stations spaced 400 m apart in the central part of the profile (close to the borehole), with the spacing increasing to 800 m

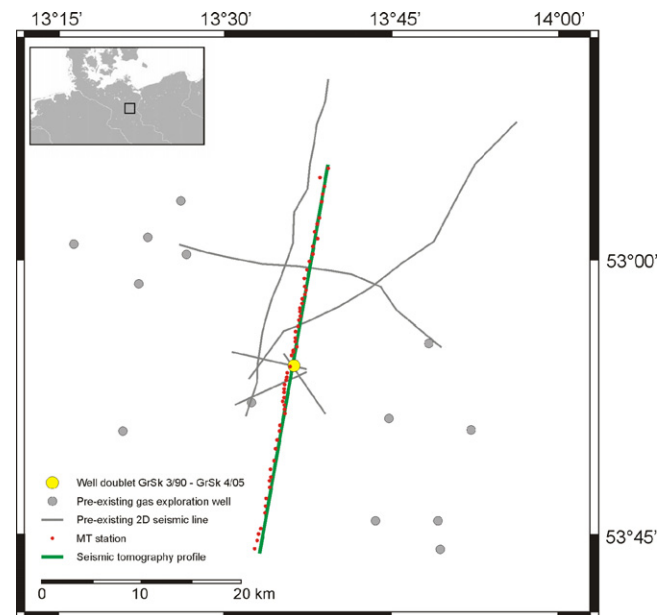


Fig. 3. Groß Schönebeck geothermal test site. Grey dots and lines show the location of existing wells and of the 2D seismic sections used to derive the 3D geologic model (Fig. 2 and Moeck et al., 2008). Red dots and the green line show the location of the MT stations and the seismic tomography profile.

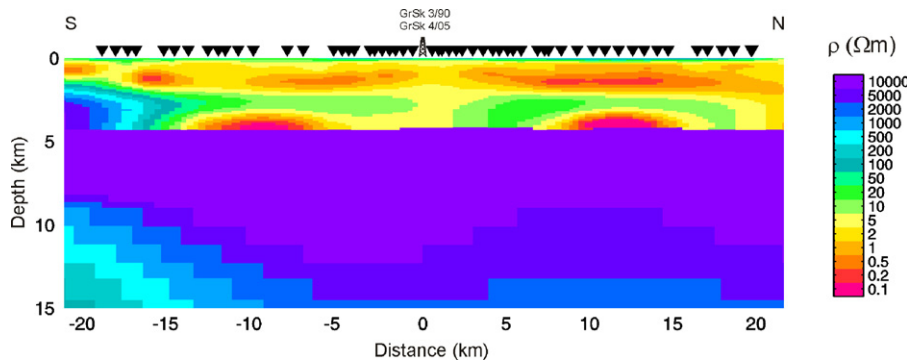


Fig. 4. Electrical resistivity model obtained from the tear zones inversion of the magnetotelluric data (Muñoz et al., submitted for publication) using a high-resistivity basin floor as *a priori* information from the high-velocity basement in the seismic velocity model. Inverted triangles indicate locations of MT stations. The location of the cross-section is shown by the green line in Fig. 2.

towards both of its ends. The frequency of the observations was in the 0.001–1000 Hz range. The MT profile is spatially coincident with the seismic tomography profile and most of the stations were located at the same places as the seismic shot points. At all sites, we recorded horizontal electric and magnetic field components and the vertical magnetic field.

Given the location of the survey area, approximately 20 km north of the outskirts of Berlin, with high EM noise levels, a long recording time (about six days) was necessary to improve the statistical properties of the collected data. To further improve data quality, four additional MT stations at distances between 70 and 130 km from the profile were installed to be used for remote reference processing. The geomagnetic and impedance tensor transfer functions were obtained using the robust processing algorithm described in Ritter et al. (1998) and Weckmann et al. (2005), with modifications by Krings (2007). For comparison, the data were also processed using the remote reference code of Egbert (1997).

To analyze dimensionality and directionality the data we used the code of Becken and Burkhardt (2004), which examines the impedance tensor in terms of polarization states of the electric and magnetic fields. By analyzing ellipticity of the field polarization, the regional strike direction can be identified even if galvanic distortion is present. Strike directions lie in a narrow range around 70°W (70% of the stations have strike directions between N65W and N75W), thereby indicating a mainly 2D resistivity structure. This is consistent with a multi-period, multi-site analysis of the regional strike, which also results in a direction of N70W, and close to being perpendicular to the profile (N20E). This means that the MT data are dominated by regional 2D structures and, hence, 2D inversion of the data is appropriate.

Prior to the inversion and according to the dimensionality analysis, all data of the main profile were rotated to -70° . The 2D

inversion of the MT data was performed using the algorithm of Rodi and Mackie (2001). For the inversion procedure we used both TE and TM modes of apparent resistivity and phases and real and imaginary parts of the geomagnetic transfer functions, in the 0.001–1000 Hz frequency range. We obtained a RMS (root mean square) misfit of 2.26 when employing an error floor of 10% for the apparent resistivities, 5% for the phases (equivalent to 1.5°) and 0.05 for the geomagnetic transfer functions. The starting model consists of a 1000 Ω m half-space for depths greater than 4.6 km, and 100 Ω m for shallower depths. Both areas correspond to two different tear zones. The inversion code of Rodi and Mackie (2001) allows dividing the model space into different regions (tear zones) where the model norm is minimized independently without interaction between them. This way, strong resistivity contrasts between tear zones are not penalized by the regularization of the inversion procedure.

The resistivity model for the main profile (Fig. 4) shows a conductive layer extending from the surface down to about 4 km depth, with an anti-form-type shape below the central part of the profile. At

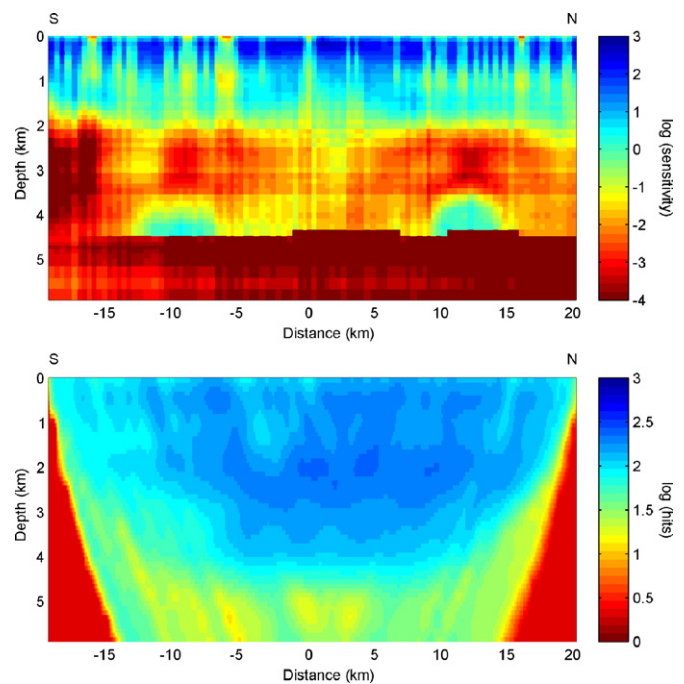


Fig. 6. Sensitivity (top panel) and hit-count distribution (bottom panel) for the MT and seismic models. These values are used to determine the error associated to each cell in the calculation of the joint probability density function. The location of the cross-sections is shown by the green line in Fig. 2.

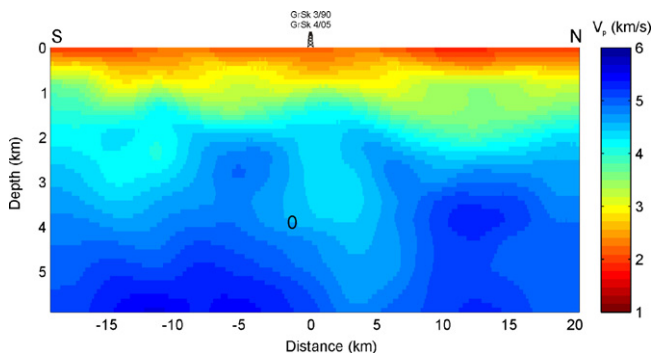


Fig. 5. Seismic velocity (V_p) model obtained from travel time inversion. The location of the cross-section is shown by the green line in Fig. 2.

the 4–5 km depth range two conductive bodies are found, separated by a region of moderate resistivity. A high-resistivity basin floor underlies the model. The strong resistivity contrast represented by the basin floor was introduced based on the seismic tomography (see below and Fig. 5) that shows high-velocity values for depths greater than 4 km. Furthermore, the pre-Permian basin floor in this region of the NEGB is represented by Lower Carboniferous Flysch facies, which is typically associated with high resistivity (Hoffmann et al., 2005).

A striking feature of the resistivity model is the moderate resistivity associated with the Zechstein evaporites. Salt domes in the NEGB usually appear as high-resistivity bodies in the MT data. However, the evaporites in the study area are made up of claystones (2.3%), carbonates (1.3%), anhydrite (6.6%) and salt rock (89.8%), as identified from borehole cuttings. Core logs and drill cuttings (no resistivity logs are available) show interstratified gypsum layers in the salt rock sections and salt-filled fractures in the brittle carbonates and anhydrites, indicating brine circulation at some times. In this context, the bulk resistivity of the lithologically heterogeneous Zechstein evaporites is lower than the values usually found in the literature for salt rocks.

Several tests were performed to check whether a high-resistivity anomaly located at the Upper Permian level would be compatible with the measurements. However, the tests clearly indicate that placing a high-resistivity body at the location of the drilled salt body results in a significantly larger data misfit. All inversion tests generate resistivity models showing a moderately

resistive dome. Therefore, we conclude that both the trapped fluids within the fractured carbonates and anhydrites, and the clay minerals contribute to a lower resistivity of the evaporitic layers than would be expected for salt rock structures. Sensitivity tests studying the depth of the basin floor represented by the strong resistivity contrast (horizon H6 in Fig. 2) indicate that it represents a minimum depth for the basin floor. Resolution tests of the deep conductive anomalies show that their presence and location is well resolved, but that their shape is subject to uncertainty based on the available data. For further details about the electrical resistivity model and sensitivity and resolution tests see Muñoz et al. (submitted for publication).

3.2. Seismic tomography model

A 40 km long seismic profile was measured coincident with the MT experiment (Fig. 3). The objective was to derive a regional 2D seismic model that could be combined with the electrical resistivity model obtained from the MT data analysis in order to study the potential reservoir and overlying layers. The experimental setup was designed to provide data suitable for refraction tomography. Forty-five explosion shots were fired from 20 m deep boreholes using 30 kg charges; the shot spacing was 800 m on average. The recording instrumentation consisted of 4.5 Hz three-component geophones. These were deployed as a 40 km long receiver spread with 200 m spacings; all receivers recorded each shot. Maximum offsets vary between 20 and 40 km depending on shot location. A

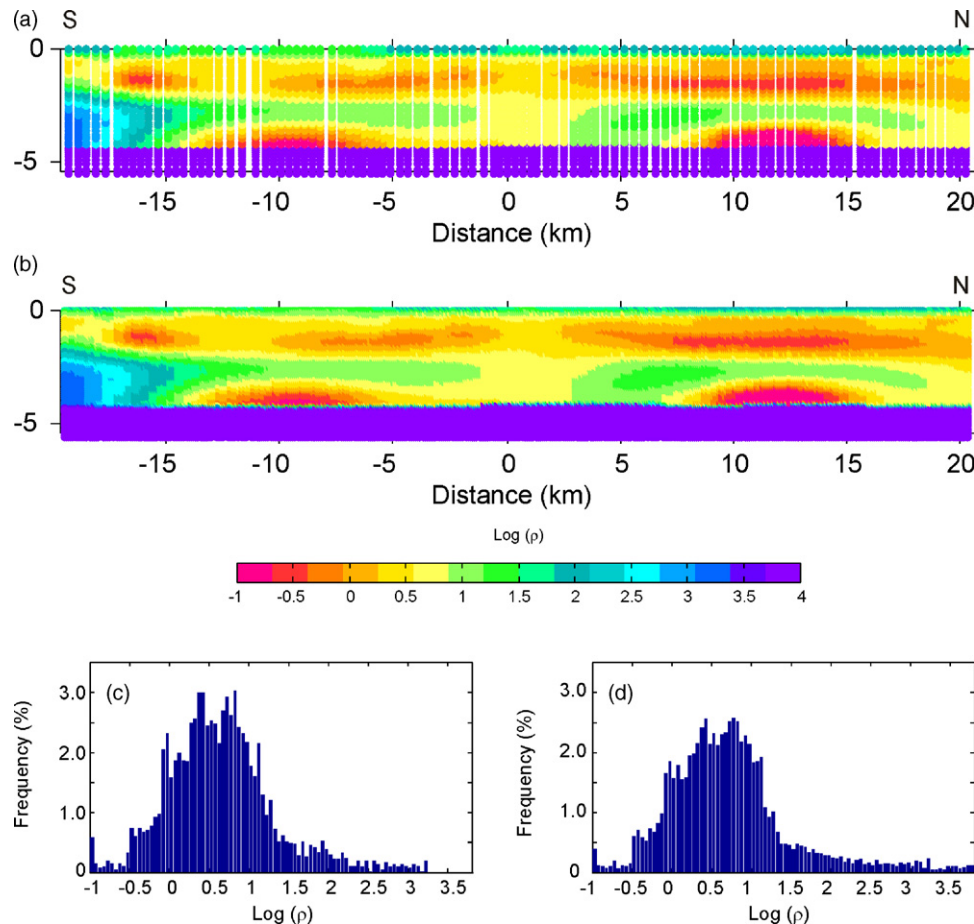


Fig. 7. Original (a) and interpolated (b) electrical resistivity models. Only the centres of the cells are depicted in order to show the irregular grid used in the MT model. The histograms of the resistivity distributions for the original (c) and interpolated (d) models show that the interpolation is not introducing any artificial structures while keeping as much information as possible. In both histograms, the peak around a resistivity of 10⁴ Ω m (resistive lower part of the models) is not shown for greater clarity. The location of the cross-sections is shown by the green line in Fig. 2.

best fitting line along the source and receiver stations was determined in order to site the 2D cross-section.

For the purpose of refraction tomography analysis, the initial data processing included installation geometry, trace editing, band-pass filtering, frequency–wave number filtering, and deconvolution. First arrival travel times were determined for all 45 shots resulting in a data set of approximately 6200 travel time picks. On average, the travel times were determined with estimated uncertainties of 30 ms based on a multiple picking approach (Bauer et al., submitted for publication). These data were used to develop a P-wave velocity model along the profile.

The first step of the model reconstruction was the search for an optimum 1D structure that was parameterized by the velocity at the surface and the vertical velocity gradient. A systematic search for the optimal combination of these two parameters was carried out by forward modelling (Zelt and Smith, 1992) and by analyzing the resulting error function (Bauer et al., 2003). Following this, the best 1D parameter set was used to build the starting model for the 2D tomography analysis.

The SIMULPS damped least-squares algorithm (Thurber, 1983) was employed to invert the travel time data and derive a 2D velocity model (Fig. 5). In addition, the FAST package of Zelt and Barton (1998) was applied to the data set. Both methods provided comparable velocity models. The disagreement was less than 2%, evidence of the robustness of the velocity model shown in Fig. 5 with respect to the inversion methodology. As an illustration of the spatial variation in uncertainty of the velocity model, the bottom panel of Fig. 6 shows the distribution of the ray-hit counts per tomography cell ($100 \text{ m} \times 100 \text{ m}$). This information was further used in the statistical analysis of the combined seismic and MT cross-section.

The velocity model can be divided into three major sequences: The upper section (depth range: 0–2 km) is characterized by low velocities (2–3.5 km/s) and a rapid velocity increase with depth. The section between 2 and 4 km depth shows velocities between 4 and 4.5 km/s and presents a significant variation in the topography of its upper surface due to salt mobility. The salt pillows are characterized by reduced velocities compared with the undisturbed surroundings, which is most likely related to increased strain and fracturing caused by the tectonic deformation of the salt bodies (Popp and Kern, 1998; Bauer et al., submitted for publication). The third and deepest section is bound on top by a sub-horizontal interface at 4.2 km depth, and has velocities higher than 5 km/s. More details on the data processing, velocity tomography and uncertainty analysis can be found in Bauer et al. (submitted for publication).

4. Joint analysis

4.1. Interpolation

As discussed in Section 2, the first step of the joint analysis is the interpolation of both data sets onto a common grid. In order to minimize the number of interpolations and avoid losing information, the electrical resistivity model was interpolated onto the seismic tomography grid. For comparison, both the original and interpolated resistivity models, together with the point distribution histograms, are shown in Fig. 7.

The interpolation was performed using an inverse distance weighted (IDW) scheme. Several weights and buffers (see Section 2.1) were tested and compared with the initial point distribution by cross-validation, which is performed by removing model points and using the neighbouring samples to estimate the value at the interpolation point. The residuals, i.e. the difference between the initial and estimated point distributions, provide a measure of the accuracy of the interpolation.

The histograms of the initial and interpolated resistivity models were also checked to ensure that the relative frequency of the dif-

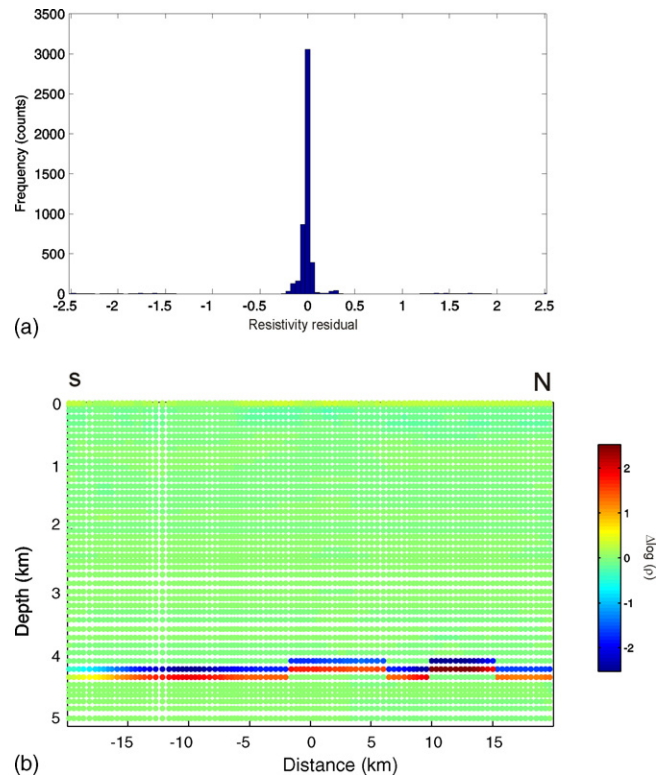


Fig. 8. Cross-validation study. (a) Distribution of residual resistivities $[\log(\rho_{\text{interpolated}}) - \log(\rho_{\text{original}})]$ and (b) spatial distribution of resistivity residuals. The figure shows that the chosen interpolation scheme produces minimal discrepancies between the original and interpolated models, with high residuals confined to the cells adjacent to where there is strong resistivity contrast. The location of the cross-section is shown by the green line in Fig. 2.

ferent parameters does not change significantly in the interpolation process. In our case, the best results were achieved using a buffer zone that increased with depth, and weights related to the square distance to the interpolation point. The residuals (Fig. 8) are small and centred at zero, indicating a good correspondence between the initial resistivity model and the interpolated one. The largest residuals correspond to the areas adjacent to the strong resistivity contrast at the basin floor. Given the big differences in resistivity above and below that interface, some amount of smoothing is inherent in the interpolation scheme. Nevertheless, the few cells that are affected have low statistical significance and barely modify the joint pdf.

4.2. Model correlation

Having both data sets on a common grid, we can now represent the joint model space in a velocity–resistivity cross-plot, and together with error estimates for each of the parameters, calculate the joint pdf according to Eqs. (1) and (2). In order to estimate the errors of ρ_a and V_p , according to Eqs. (3) and (4) we use the normalized sensitivity and hit-count distributions, respectively (Fig. 6). The mean errors $C_{\log(\rho)}$ and C_{V_p} are estimated from the scatter plot of velocity versus log resistivity and have been chosen as 0.1 (10%) for ρ and 0.1 km/s for V_p . The joint pdf is shown in Figs. 9a and b.

4.3. Classification

In the pdf plots of Fig. 9 we can identify five distinct peaks, or areas of enhanced probability with respect to their neighbouring regions. These areas are represented by a number of bivariate

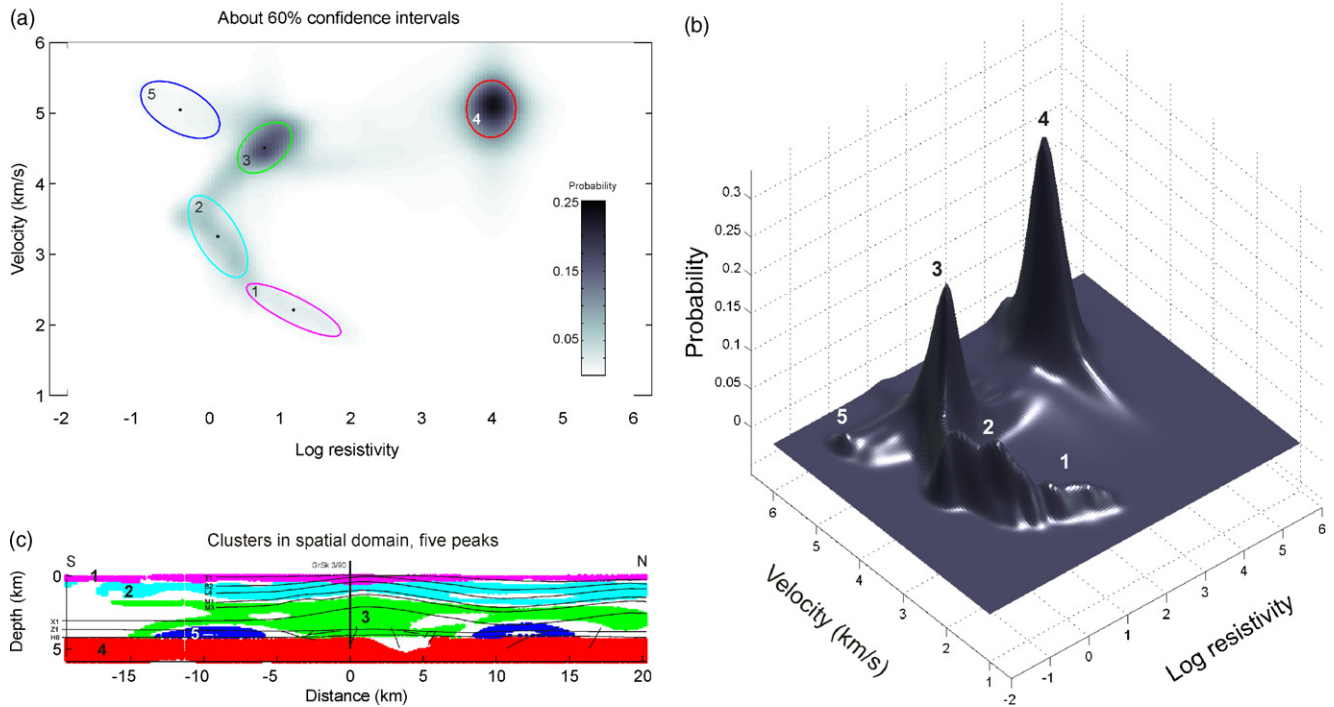


Fig. 9. Cross-plot of the probability density function in gray-scale (a) plan view and (b) 3D view. Panel (c) shows the spatial distribution of classes; the location of the cross-section is shown by the green line in Fig. 2. Colours correspond to the ellipses in (a) defining the class boundaries. See Fig. 2 for the seismic horizons and text for further details.

Table 1

Resistivities and seismic P-velocities for the five classes defined by this study (see Fig. 9), and corresponding lithologies and stratigraphic units.

Class	ρ (Ω m)	V_p (km/s)	Lithology	Stratigraphic unit(s)
1	5–70	1.8–2.7	Unconsolidated sediments (sands, gravels, clays)	Cenozoic
2	0.5–3.5	2.7–3.9	Clays, marls, marly limestones, limestones, sandstones	Cretaceous–Upper Triassic
3	2–15	4–5	Brittle limestones, sandstones, evaporites	Middle Triassic–Lower Permian
4	$3\text{--}30 \times 10^3$	4.7–5.5	Volcanic rocks, quartzites, slates	Lower Permian–Carboniferous
5	0.1–0.7	4.7–5.5	Anhydrite	Lower Permian

Gaussian functions that are used as starting values for the non-linear least-squares fitting of Eq. (5). The coloured ellipses in Fig. 9a represent the $\sim 60\%$ confidence intervals (defined as the full width at half maximum value) of the Gaussian peaks best fitting the pdf according to Eq. (5), except for ellipse 5 (blue), which is plotted using the starting (manually picked) values instead of the fitted ones. Using the best fit peaks, Classes 3 and 5 overlap significantly indicating that under the assumption of the multi-Gaussian pdf, these two classes cannot be separated. However, visual inspection of the pdf (Fig. 9b) shows that the peak around ellipse 5 represents an area of enhanced probability with distinct velocity and resistivity with respect to Class 3. For this reason we chose to override the best fitting peak with a manually selected one. The chosen class distribution is in excellent agreement with the calculated pdf in most of the parameter space, while allowing a unique spatial mapping (Fig. 9c).

The shallowest class (Class 1) is characterised by low velocity (1.8–2.7 km/s) and moderate resistivity (5–70 Ω m). Class 2, underlying the former, has higher velocities (2.7–3.9 km/s) and lower resistivities (0.5–3.5 Ω m). Class 3 is characterised by even higher velocities (4–5 km/s), but also slightly higher resistivities (2–15 Ω m). Class 4, the deepest one, has the highest velocity (4.7–5.5 km/s) and resistivity (about 3000–30,000 Ω m) values. Compared to the other classes, Class 5 has a limited spatial extension and is characterized by high velocities (4.7–5.5 km/s) and extremely low resistivities (0.1–0.7 Ω m). These resistivity and velocity values are summarised in Table 1, which includes the inter-

preted lithologic and/or geologic types, as described in the next section.

5. Discussion and conclusions

The MT and seismic data were used to derive 2D models of the electrical resistivity and the seismic P-wave velocity in the vicinity of the Groß Schönebeck research wells GrSk 3/90 and GrSk 4/05. The two models were combined and a statistical analysis was carried out to determine correlating features in both data sets. The classification method used in this analysis revealed five distinct litho-types that show up as separate clusters in the defining geophysical parameter space. The clusters were mapped back onto the cross-section providing a depth distribution of the litho-types along the profile shown in Fig. 9c. In order to interpret the nature of the various litho-types, the model was superimposed onto the stratigraphy known from pre-existing reflection seismic data and borehole information (Moeck et al., 2008). This way, the different classes in the seismic velocity–electrical conductivity cross-plot can be related to lithologic units of the NEGB.

Class 1 comprises unconsolidated sediments like sands, gravels and clays. It is bound by the seismic reflector horizon T1 (Fig. 9c), which correspond to the bottom of the Cenozoic sequence. These, unconsolidated, porous sediments have a low-velocity-moderate resistivity signature (see Table 1). Class 2 extends between seismic reflector horizons T1 to M1 (Fig. 9c) encompassing sediments and weak or soft rocks like clays, marls, marly limestones, and some thin

layers of limestones and sandstones of Cretaceous to Upper Triassic age. These materials have relatively high porosity and, therefore, high fluid content. In addition, clay conductivity (cation exchange capacity) also plays an important role, resulting in lower bulk resistivity than Class 1.

Class 3, between seismic reflector horizons M1 to H6 (Fig. 9c), coincides with the Middle Triassic to Lower Permian sequence that is dominated by harder, brittle, lower porosity limestones and sandstones, as indicated by their higher resistivities and seismic velocities (Table 1). This class also includes thick evaporitic layers (Zechstein), made up of salt rock, claystones, and fractured carbonates and anhydrite. Both the bulk resistivity and velocity of the Zechstein evaporites are significantly lower than those mentioned in the literature for this type of sedimentary rocks, making their properties, at scales resolved by MT and seismic methods, generally similar to those of the limestones and sandstones included in Class 3.

Class 4 represents the basin floor, bound at the top by seismic reflector H6 (Fig. 9c) and comprises Lower Permian to Carboniferous volcanic rocks, quartzites and slates. The Carboniferous, in this part of the NEGB, is primarily represented by flysch facies with a high-resistivity signature (Hoffmann et al., 2005). This class reflects the fact that, in the construction of the MT model, a high-resistivity basin floor was introduced based on information obtained from the seismic model. Therefore, there is a high correlation between velocity and resistivity producing such a high peak for this particular class (Fig. 9b).

Class 5 appears to be more structurally controlled, as it does not coincide with seismic reflector horizons. It is remarkable that this class is restricted to thin evaporites where, presumably, Upper Permian anhydrites remain after salt mobilization. These anhydrites, in contrast to the more plastic evaporites that formed the upwellings, are brittle and are expected to be highly fractured. The modelled 0.1–0.7 Ωm resistivities can be explained by using Archie's Law (Archie, 1942) for fracture-controlled porosity and by assuming a formation fluid salinity of 260 g/l (Giese et al., 2001) and a reasonable range of porosities and temperatures (see Ollinger et al., 2010). The large seismic velocities reflect the high density of anhydrite (2.9 g/cm³).

The joint model derived with our combined approach to the analysis of MT resistivity and seismic velocity data allows visualizing local rock classifications in a manner that can be directly applied to the exploration of deep geothermal reservoirs. However, the geologic interpretation of these joint models and geophysical parameters is still affected by uncertainty. Investigations at other sites and comparisons to well data will help clarify such issues. Nevertheless, the systematic integration of different geophysical methods such as MT and seismic, when combined with geological constraints, is a promising approach to geothermal exploration.

Acknowledgments

This work was funded within the 6th Framework Program of the European Union (I-GET Project, Contract no. 518378). The instruments for the geophysical experiments were provided by the Geophysical Instrument Pool Potsdam (GIPP). We wish to thank Paul Bedrosian for making his statistical analysis code available to us. This paper was greatly improved by the comments of W. Cumming, M. Hoversten, M. Lippmann and M. Virgilio.

References

- Archie, G., 1942. The electrical resistivity log as an aid in determining some reservoir characteristics. *Trans. Am. Inst. Min. Metall. Pet. Eng.* 146, 54–62.
- Bauer, K., Schulze, A., Ryberg, T., Sobolev, S.V., Weber, M., 2003. Classification of lithology from seismic tomography: a case study from the Messum igneous complex, Namibia. *J. Geophys. Res.* 108, doi:10.1029/2001JB001073.
- Bauer, K., Moeck, I., Norden, B., Schulze, A., Weber, M. Tomographic P velocity and gradient structure across the geothermal site Gross Schoenebeck (NE German Basin): relationship to lithology, salt tectonics, and thermal regime. *J. Geophys. Res.*, submitted for publication.
- Becken, M., Burkhardt, H., 2004. An ellipticity criterion in magnetotelluric tensor analysis. *Geophys. J. Int.* 159, 69–82.
- Bedrosian, P.A., Maercklin, N., Weckmann, U., Bartov, Y., Ryberg, T., Ritter, O., 2007. Lithology-derived structure classification from the joint interpretation of magnetotelluric and seismic models. *Geophys. J. Int.* 170, 737–748.
- Bedrosian, P.A., Unsworth, M.J., Egbert, G.D., Thurber, C.H., 2004. Geophysical images of the creeping segment of the San Andreas fault: implications for the role of crustal fluids in the earthquake process. *Tectonophysics* 385, 137–158.
- Bosch, M., 1999. Lithologic tomography: from plural geophysical data to lithology estimation. *J. Geophys. Res.* 104, 749–766.
- Colombo, D., Mantovani, M., Hallinan, S., Virgilio, M., 2008. Sub-basalt depth imaging using simultaneous joint inversion of seismic and electromagnetic (MT) data: a CRB field study. In: 78th Annual International Meeting of the SEG, 9–14 November, Las Vegas, NV, USA, Expanded Abstracts, pp. 2674–2678.
- Egbert, G.D., 1997. Robust multiple-station magnetotelluric data processing. *Geophys. J. Int.* 130, 475–496.
- Gallardo, L.A., Meju, M.A., 2007. Joint two-dimensional cross-gradient imaging of magnetotelluric and seismic travel-time data for structural and lithological classification. *Geophys. J. Int.* 169, 1261–1272.
- Giese, L., Seibt, A., Wiersberg, T., Zimmer, M., Erzinger, J., Niedermann, S., Pekdeger, A., 2001. Geochemistry of the formation fluids. In: 7. Report der Geothermie Projekte, In situ-Geothermieslabor Groß Schönebeck 2000/2001 Bohrarbeiten, Bohrlochmessungen, Hydraulik, Formationsfluide, Tonminerale. GFZ Potsdam report No. STR02/14, Potsdam, Germany, pp. 145–169 (in German).
- Haberland, C., Rietbrock, A., Schurr, B., Brasse, H., 2003. Coincident anomalies of seismic attenuation and electrical resistivity beneath the southern Bolivian Altiplano plateau. *Geophys. Res. Lett.* 30, doi:10.1029/2003GL017492.
- Hoffmann, N., Jödicke, H., Horeshschi, L., 2005. Regional distribution of the Lower Carboniferous Culm and Carboniferous limestone facies in the North German Basin – derived from magnetotelluric soundings. *Zeitschrift der Deutschen Gesellschaft für Geowissenschaften* 56 (2), 323–339.
- Hoversten, G.M., Chen, J., Gasperikova, E., Newman, A., 2005. Integration of marine CSEM and seismic AVA data for reservoir parameter estimation. In: 75th Annual International Meeting of the SEG, 6–11 November, Houston, TX, USA, Expanded Abstracts, pp. 579–582.
- Isaaks, E., Srivastava, R., 1989. *Applied Geostatistics*. Oxford University Press, New York, NY, USA, 572 pp.
- Jones, A.G., 1987. MT and reflection: an essential combination. *Geophys. J. R. Astron. Soc.* 89, 7–18.
- Jones, A.G., 1998. Waves of the future: superior inferences from collocated seismic and electromagnetic experiments. *Tectonophysics* 286, 273–298.
- Krings, T., 2007. The influence of robust statistics, remote reference, and a criterion based on horizontal magnetic transfer functions on MT data processing. Diploma Thesis, WWU Münster – GFZ Potsdam, Germany, 108 pp.
- Maercklin, N., Bedrosian, P.A., Haberland, C., Ritter, O., Ryberg, T., Weber, M., Weckmann, U., 2005. Characterizing a large shear-zone with seismic and magnetotelluric methods: the case of the Dead Sea Transform. *Geophys. Res. Lett.* 32, doi:10.1029/2005GL022724.
- Mechie, J., Sobolev, S.V., Ratschbacher, L., Babeyko, A.Y., Bock, G., Jones, A.G., Nelson, K.D., Solon, K.D., Brown, L.D., Zhao, W., 2004. Precise temperature estimation in the Tibetan crust from seismic detection of the α - β quartz transition. *Geology* 32, 601–604.
- Moeck, I., Schandlmeier, H., Holl, H.G., 2008. The stress regime in Rotliegend reservoir of the Northeast German Basin. *Int. J. Earth Sci. (Geol. Rundsch.)*, doi:10.1007/s00531-008-0316-1.
- Moorkamp, M., Jones, A.G., Eaton, D.W., 2007. Joint inversion of teleseismic receiver functions and magnetotelluric data using a genetic algorithm: Are seismic velocities and electrical conductivities compatible? *Geophys. Res. Lett.* 34, doi:10.1029/2007GL030519.
- Muñoz, G., Ritter, O., Moeck, I. A target-oriented magnetotelluric inversion scheme for characterizing the low enthalpy Groß Schönebeck geothermal reservoir. *Geophys. J. Int.*, submitted for publication.
- Ollinger, D., Baujard, C., Kohl, T., Moeck, I., 2010. Distribution of thermal conductivities in the Groß Schönebeck (Germany) test site based on 3D inversion of deep borehole data. *Geothermics* 39, 46–58.
- Popp, T., Kern, H., 1998. Ultrasonic wave velocities, gas permeability and porosity in natural and granular rock salt. *Phys. Chem. Earth* 23, 373–378.
- Ritter, O., Junge, A., Dawes, G., 1998. New equipment and processing for magnetotelluric remote reference processing. *Geophys. J. Int.* 132, 535–548.
- Rodi, W., Mackie, R.L., 2001. Nonlinear conjugate gradients algorithm for 2-D magnetotelluric inversions. *Geophysics* 66, 174–187.
- Scheck, M., Bayer, U., 1999. Evolution of the Northeast German Basin—Inference from structural model and subsidence analysis. *Tectonophysics* 313, 145–169.
- Scheck, M., Barrio-Alvers, L., Bayer, U., Götze, H.J., 1999. Density structure of the Northeast German Basin: 3D modelling along the DEKORP line BASIN96. *Phys. Chem. Earth* 24, 221–230.
- Schwalenberg, K., Rath, V., Haak, V., 2002. Sensitivity studies applied to a two-dimensional resistivity model from the Central Andes. *Geophys. J. Int.* 150, 673–686.
- Thurber, C.H., 1983. Earthquake locations and three-dimensional crustal structure in the Coyote Lake area, Central California. *J. Geophys. Res.* 88, 8226–8236.

- Unsworth, M.J., Bedrosian, P.A., 2004. Electrical resistivity structure at the SAFOD site from magnetotelluric exploration. *Geophys. Res. Lett.* 31, doi:10.1029/2003GL019495.
- Unsworth, M.J., et al., 2005. Crustal rheology of the Himalaya and Southern Tibet inferred from magnetotelluric data. *Nature* 438, 78–81.
- Vozoff, K., 1987. The magnetotelluric method. In: Naibighian, M. (Ed.), *Electromagnetic Methods in Applied Geophysics*. Society of Exploration Geophysics, Tulsa, OK, USA, pp. 641–711.
- Weckmann, U., Magunia, A., Ritter, O., 2005. Effective noise separation for magnetotelluric single site data processing using a frequency domain selection scheme. *Geophys. J. Int.* 161, 456–468.
- Zelt, C.A., Barton, P.J., 1998. Three-dimensional seismic refraction tomography: a comparison of two methods applied to data from the Faeroe Basin. *J. Geophys. Res.* 103 (B4), 7187–7210.
- Zelt, C.A., Smith, R.B., 1992. Seismic traveltime inversion for 2-D crustal velocity structure. *Geophys. J. Int.* 108, 16–34.